An Advanced Hexacopter for Mars Exploration: Attitude Control and Autonomous Navigation

LAURA SOPEGNO
University of Denver, Denver, CO USA
University of Palermo, Palermo, Italy

SIMONE MARTINI
University of Denver, Denver, CO USA

SALVATORE PEDONE, Member, IEEE
ADRIANO FAGIOLINI, Member, IEEE
University of Palermo, Palermo, Italy

MATTHEW J. RUTHERFORD, Member, IEEE
MARGARETA STEFANOVIC, Senior Member, IEEE
University of Denver, Denver, CO USA

ALESSANDRO RIZZO, Senior Member, IEEE
Polytechnic of Turin, Turin, Italy

PATRIZIA LIVRERI, Senior Member, IEEE
University of Palermo, Palermo, Italy

KIMON P. VALAVANIS, Senior Member, IEEE
University of Denver, Denver, CO USA

Manuscript received 13 October 2023; revised 26 January 2024; accepted 6 February 2024. Date of publication 13 February 2024; date of current version 11 June 2024.

DOI. No. 10.1109/TAES.2024.3365667

Refereeing of this contribution was handled by A.L'Afflitto. *(Laura Sopegno and Simone Martini are first authors with equal contribution. Patrizia Livreri, and Kimon P. Valavanis are co-last authors with equal contribution.)*

Authors' addresses: Laura Sopegno, Simone Martini, Matthew J. Rutherford, Margareta Stefanovic, and Kimon P. Valavanis are with the Department of Electrical and Computer Science, University of Denver, Denver, CO 80210, USA, E-mail: (laura.sopegno@du.edu; simone.martini@du.edu; Matthew.Rutherford@du.edu; Margareta.Stefanovic@du.edu; kimon.valavanis@du.edu); Laura Sopegno, Salvatore Pedone, Adriano Fagiolini, and Patrizia Livreri are with the Department of Electronic Engineering, University of Palermo, 90133 Palermo, Italy, E-mail: (laura.sopegno@du.edu; salvatore.pedone@unipa.it; adriano.fagiolini@unipa.it; patrizia.livreri@unipa.it); Alessandro Rizzo is with the Polytechnic of Turin, 10129 Turin, Italy. *(Corresponding authors: Laura Sopegno; Simone Martini; Patrizia Livreri; Kimon P. Valavanis.)*

Mars exploration has recently witnessed major interest within the scientific community, particularly because unmanned aerial robotic platforms offer reliable alternatives for acquiring and collecting data and information from the Red Planet. However, the specific conditions of the Martian environment result in a restricted flight envelope when flying close to Mars and then landing on the surface of Mars. Therefore, in addition to the requirement to develop an aerial platform suitable for operations on Mars, autonomous navigation strategies and robust controllers are also needed for exploration tasks. It is argued that hexacopters with their relatively compact design represent a promising solution for autonomous exploration tasks on Mars, overcoming at the same time the limitations of wheel-based rovers. This research focuses on the design of a Mars hexacopter for a scouting mission in the Jezero region of Mars. The configuration and architecture of the hexacopter follow NASA conceptual study of the Mars science helicopter. Then, the mission profile for mapping the Belva crater is examined, followed by a detailed approach to implement and test observer-based navigation and control strategies. A comprehensive simulated experiments environment based on the integration of robot operating system and Ardupilot is also presented, used to validate the overall system architecture and mission parameters considering both the morphological shape of the explored crater and the atmospheric conditions of Mars.

I. INTRODUCTION

Unmanned missions for space exploration have emerged during the last two decades. Missions in Mars dominate the scientific interest as evidenced by the NASA Mars 2020 [1] project. In the most recent mission, the overall system included a robotic rover, Perseverance, and a small Mars helicopter (MH), Ingenuity [2], [3] that were used to explore the Red Planet and look for signs of past life. The successful Ingenuity flights underlie the importance of UAVs when it comes to extraterrestrial exploration, and support the use of rotorcrafts in complex scenarios, such as the Mars sample return (MSR) mission [4], [5], [6], where two helicopters may contribute to the transportation of terrain samples in collaboration with the rover's activity. Moreover, completion of such significant missions paves the way to future manned–unmanned exploration missions [7].

However, the current MH configuration has neither a specific scientific payload (P/L) nor enhanced onboard sensors, thus, limiting its capabilities to short flights over relatively flat and rock-free terrains [2]. Considering as a reference baseline the recent study of NASA Jet Propulsion Laboratory (JPL) and the Ames Research Center on the Mars science helicopter (MSH) [8], this research provides an in-depth analysis of an enhanced Mars hexacopter (MHex) configuration, which includes shape and size of the main subsystems, as well as autonomous navigation and control strategies. The choice of a six-rotor rather than a quadrotor configuration is preferred because hexacopters demonstrate better stability, redundancy, payload capacity, and increased lifting power. Communication delays between the Earth and Mars cannot guarantee a continuously direct link for real-time data transfer, commands, and operations. For this reason, it is realistic to consider that: 1) the MHex will receive limited (transmitted-encoded) commands from the ground control station (GCS); 2) the MHex will be able to autonomously navigate and execute specific tasks/missions

in a GPS-denied environment; and 3) the MHex will maintain a stable attitude along its trajectory relying only on its onboard guidance, navigation and control (GNC) system.

The objectives and aims of this research center around: 1) providing an accurate model for the proposed MHex. Sizing onboard sensors, tracking camera, 3-D LiDAR, and other equipment of the MHex are based on available data from [9], [10], and [11]; 2) developing a simulator architecture for both the Martian environment and simulated experiments by integrating robot operating system (ROS), Gazebo, and Ardupilot, which allows for implementation and testing of simultaneous localization and mapping (SLAM), navigation, and control algorithms; and 3) defining a specific mission profile for which SLAM and autonomous navigation strategies are developed. As such, implementation of the unknown input observer (UIO) [12] is adopted to estimate the MHex states and unknown disturbances that act on the system [13], [14], [15], [16], [17], [18]. Note that due to the atmospheric conditions on Mars [19], [20], the MHex flight envelop challenge is tackled by implementing model-based controllers for better trajectory tracking accuracy when compared to the default Ardupilot PID controller [21].

The rest of this article is organized as follows. Section II defines the mission requirements according to the Mars atmospheric conditions, as well as the design and size of the MHex. Section III presents the onboard GNC system and the overall architecture of the simulator tool. Obtained results are given in Section IV. Finally, Section V concludes this article.

II. MISSION PROFILE AND SYSTEM DESIGN

This section describes the mission profile of the MHex under the Martian atmospheric conditions in the Jezero region, where the Belva crater is located, together with the architecture of the hexacopter system.

A. Mars Atmosphere

The Martian atmosphere limits flight conditions and, in turn, the configuration of aerial vehicles. Because of such atmospheric conditions and composition, oxidizing power sources cannot be used, and the gravitational acceleration g and atmospheric density ρ become the driving factors in lift generation. The low-density that reflects low Reynolds numbers, Re, in the range between 10 000–25 000, impacts significantly the airfoil design and aerodynamic performance, and suggests the use of lightweight materials for the hexacopter structure. Furthermore, the lower sound speed limits the rotors' maximum rotational speed. Table I compares the Earth and Mars atmosphere, also considering the atmospheric conditions of the Jezero region, which impact the design and analysis of the MHex. The sound speed on Mars refers to a Mach number (M) of 0.7.

TABLE I
Atmosphere Comparison on Earth and Mars (Jezero Region)

	Unit	Earth	Mars
Grav. acceleration, g	m/s^2	9.81	3.71
Temperature, T	K	288	223
Density, ρ	kg/m^3	1.225	0.015
Viscosity, μ	Ns/m^2	1.75×10−5	1.13×10−5
Sound speed, a	m/s	340.3	233.1
Tip speed, V_{tip}	m/s	238	163

Fig. 1. Study area of the Belva crater in the Jezero region. Image obtained from the HiRISE dataset.

B. Mission Requirements

The planned mission focuses on autonomous exploration of the Belva crater. An SLAM technique is adopted to collect data from the implemented autonomous mapping process (see Section IV). The MHex, as designed, increases the range of the examined terrain compared to traditional rovers [22], the endurance and range of which is limited because of ground obstacles and harsh terrains, such as craters and caves. Moreover, because of the near-surface flight altitude, the MHex guarantees a higher resolution than orbiters, resulting in a promising solution to better explore the Mars surface. For the mission under consideration, a 34-Km^2 area within and around the Belva crater is chosen for autonomous navigation and mapping, see Fig. 1. This area is of scientific interest [23] as this region is related to the Mars 2020 Landing site [1] and it is deemed suitable for surficial deposits of ichnofossils as morphological evidence of past biological behavior.

The whole mission consists of five segments: 1) take-off, 2) climb at the required altitude, 3) cruise, 4) descent, and 5) land (Fig. 2). The flight trajectory is based on geological waypoints sent by the ground station to the MHex. After landing and recharging for 1 sol with solar panels, the MHex is expected to continue mapping with a target scanning range of about 3 Km^2 for each flight. This represents the operative area including slight deviations from a direct course. After mapping a consistent region, the MHex returns to the lander to download the collected scientific data to optimize the onboard processor weight and power management. A

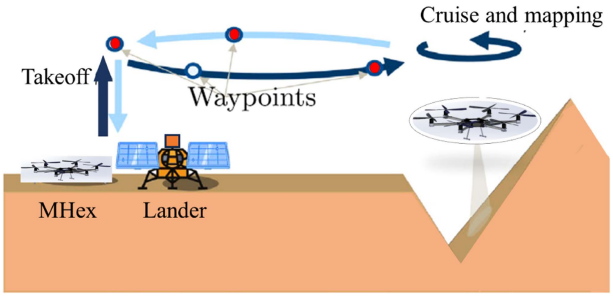

Fig. 2. MHex mission case for autonomous mapping of the Belva crater. Readapted from [24].

TABLE II
Mission Parameters for MHex-Based Autonomous Mapping

P/L	2.0 kg
Total flight area	3 Km^2
Cruise speed	up to 8 m/s
Cruise altitude	10 m

summary of the main mission parameters for the MHex is reported in Table II.

C. System Architecture

Several studies using aerial vehicles for planetary exploration have already been conducted; a summary of the proposed configurations may be found in [25] and [26]. However, findings in [27] show that a tailsitter design, which is a challenging system, have not offered any major advantage over a more conventional rotorcraft [28]. But as mentioned in Section I, the hexacopter configuration is a promising and robust design choice in this regard.

1) *Mars Hexacopter Sizing:* The MHex design process starts with the definition of the mission requirements, thus the P/L identification. The MHex design is implemented in Solidworks, and the system sizing is based on the diameter of the rotor blade which is optimized for the required thrust in the Martian atmosphere. The six motors are sized with a 150% control margin for hover power, accommodating a motor speed up to 3008 r/min. The MHex blade is derived from the fluidic analysis in [8], considering the same diamond-shaped airfoils for the blade inboard sections with an 8% thickness-to-chord ratio and flight (hover and cruise) performance for M 0.55–0.8. The reference airfoil sections are already optimized for better stall behavior and lower power during flight. To account for modeling uncertainties, the MHex design includes a contingency weight factor equal to 20%, being the overall design at an early stage. Table III summarized the MHex parameters and weights, while Fig. 3 shows the blade profile and the MHex architecture. The P/L is intended as a sensing payload, containing the 3-D LiDAR sensor for mapping the environment.

With respect to the MSH baseline [8], the whole airframe is increased (3 to 3.15 m) to better compensate for drag effects acting on the rotors when rotating.

TABLE III
MHex Design. Geometry and Weights

Parameters		Value	Unit
Airframe		**15.5**	Kg
	Structure	5.9	Kg
	Propulsion	4.3	Kg
	Avionics and equipment	2.7	Kg
	Contingency (20%)	2.58	–
P/L		**2.0**	Kg
Gross weight		**17.5**	Kg
Disk radius		0.64	m
Rotor numbers		6	–
Blades per rotor		4	–
Rotor average speed range		2483	r/min
Airframe size	*length*	3.15	m
	width	3.15	m
	height	0.50	m

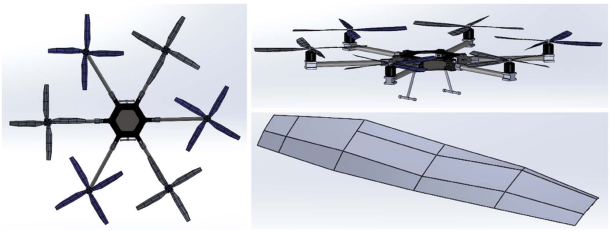

Fig. 3. *Solidworks* design of MHex structure and blade profile, 0.64-m disk radius, derived from airfoil sections in [8].

2) *Sensors:* The VLP-16 3D LiDAR [29] is chosen as the primary sensor to perform the mapping of the Belva crater. Even though cameras represent a good solution in SLAM systems, the use of LiDARs has enabled advances in the knowledge of planets, such as the Moon, Mercury, Mars, and several asteroids [30] representing a prominent technique in the future of planetary science. In 2019, a study on the geological investigation at the Lofthellir site (Iceland) was presented at the *50th Lunar and Planetary Science Conference* [31] to address the potential exploration of lava tubes on the Moon and Mars through a 3-D LiDAR-equipped drone, showing preliminary good results and a successful mapping of the cave. Furthermore, recent studies performed by NASA aim to develop advanced precision landing technologies and accurate 3-D scanning of the terrain through LiDAR-based navigation [32] to optimize the descent and landing phase of landers.

3-D LiDARs can provide structural and rich information about the scanned environment, operating efficiently in low-light/varying illumination conditions. The generated point cloud provides depth information without the need for stereo matching or depth inference by directly capturing the geometry of the environment, reducing the need for complex feature extraction algorithms required by camera-based systems. The MHex LiDAR tilting mechanism considers the exploration of both wide areas, such as craters and caves, allowing obstacle detection and collision avoidance by scanning the surrounding ground and the vertical range with a rotation of 1 Hz (Fig. 4). However, since a single-sensor SLAM system is usually fragile and full of uncertainty when performing localization, the MHex carries onboard

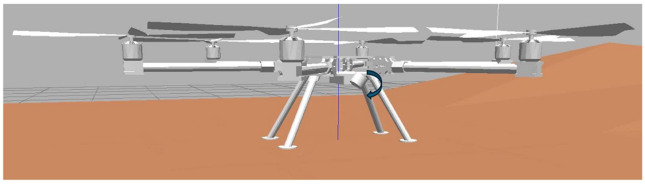

Fig. 4. MHex LiDAR tilting mechanism, Gazebo simulation.

TABLE IV
MHex Sensor Specifications

Sensor	Frequency	Power	Range	Weight
VLP-16 3D Lidar	5-20 Hz	8 W	<100 m	590 g
t265 Tracking camera	30-200 Hz	1,5 W	173°	55 g
Lite v3 Altimeter	10-30 Hz	1,3 W	<40 m	22 g

three different sensors to perform precise SLAM navigation, as further described in Section III. Table IV provides a summary of the sensor features [33], [34] used onboard the MHex.

The Garmin Lite v3 altimeter, currently used onboard the Ingenuity helicopter [35], is a light, optical distance measurement sensor that uses infrared pulses of light projected down to the ground to measure the flight altitude of the MHex with respect to the ground.

D. Simulator: High-Level Architecture

The simulation environment relies on the integration of Ardupilot, a widespread open-source autopilot system, along with the Gazebo simulator and the ROS. This combination of free and open-source tools allows for simulating the dynamic behavior of the MHex model in a Mars-like environment, accounting for high accuracy of the numerous MHex attributes, such as mass, inertia, wind gusts, and noise thus allowing it to behave realistically when simulating. Because of the complexity of the simulated mission, extensive design and some software modification are required to achieve a realistic simulation. Particularly, continuous efforts in implementing advanced control strategies and integrating control techniques into the Ardupilot system not only highlight the significant adaptability of the software but also allow researchers to develop in-depth analysis and get realistic results in complex simulation environments. Recent works considering the implementation of control strategies, such as the adaptive integral sliding mode control, as well as the adaptive control integration into the Ardupilot software, can be found in [36] and [37]. Experiments on the adaptive method for the Ardupilot-based controller can also be found in [38] for fixed-wing UAVs. For this research, the simulator runs on Ubuntu 20.04, with ROS Noetic, Gazebo 11.11.0, and Ardupilot Copter 4.3. Fig. 5 displays an overview of the resulting workflow that the simulation environment allows.

E. Mathematical Modeling

To design model-based controllers and considering the hexacopter configuration of Fig. 6 the total thrust T and torques $\tau = [\tau_\phi \tau_\theta \tau_\psi]$ can be modeled as

$$\begin{bmatrix} T \\ \tau_\phi \\ \tau_\theta \\ \tau_\psi \end{bmatrix} = \begin{bmatrix} k & k & k & k & k & k \\ -k & k & \frac{\sqrt{3}}{2}k & -\frac{\sqrt{3}}{2}k & -\frac{\sqrt{3}}{2}k & \frac{\sqrt{3}}{2}k \\ 0 & 0 & -0.5\,k & 0.5\,k & -0.5\,k & 0.5\,k \\ b & -b & b & -b & -b & b \end{bmatrix} \times \begin{bmatrix} \Omega_1^2 \\ \Omega_2^2 \\ \Omega_3^2 \\ \Omega_4^2 \\ \Omega_5^2 \\ \Omega_6^2 \end{bmatrix} \tag{1}$$

where Ω_i is the ith rotor's angular velocity while $k = 1.83\times10-4$ and $b = 2.41\times10-5$ are the thrust and drag coefficients of the propeller, respectively. These parameters are computed from hovering simulation as a result of the *LiftDrag* plugin aerodynamic effect. The complete mathematical model of the hexacopter can be obtained by considering the forces and torques of (1) into the general multirotor dynamical model

$$\ddot{p} = \frac{1}{m} T R \mathbf{e_3} - g\mathbf{e_3} \tag{2}$$

$$\ddot{\eta} = J_R^{-1}(\tau - C\dot{\eta}) \tag{3}$$

where p is the inertial position vector, m is the multirotor total mass, R is the rotation matrix from the body reference frame to the inertial reference frame which depends on the choice of Euler angles sequence $\eta = [\phi, \theta, \psi]^T$, $\mathbf{e_3} = [0, 0, 1]^T$ is the inertial z-axis vector, g the gravitational acceleration, and $J_R = W^T J W$ is the rotated inertia matrix with W being the matrix which relate angular velocities ω to Euler rates $\dot{\eta}$ and J the symmetric constant inertia matrix. C is the matrix accounting for centrifugal and Coriolis effects. The full description of the multirotor model can be found in [39].

F. Mars Hexacopter Model With ROS and Gazebo

The MHex model is exported from Solidworks to *urdf* file format, which is then converted to Gazebos's *sdf* format maintaining all inertial characteristic and meshes. The aerodynamic profile of the propellers is implemented using the *LiftDrag Plugin*, and the motor actuation from Ardupilot flight controller is managed through the *Ardupilot Gazebo Plugin*. To simulate the sensor fusion output, the odometry information is taken from an *odometry sensor* publishing up to 200 Hz. Indeed, given the Martian conditions, the global navigation satellite system (GNSS), barometer, and magnetometer would not be available. To this end, these sensors are disabled and the alternative selection of sensors from Table IV, along with the IMU, is implemented to guarantee navigation, control, and mapping functionalities. Considering the use of a rotating VLP-16 LiDAR, the

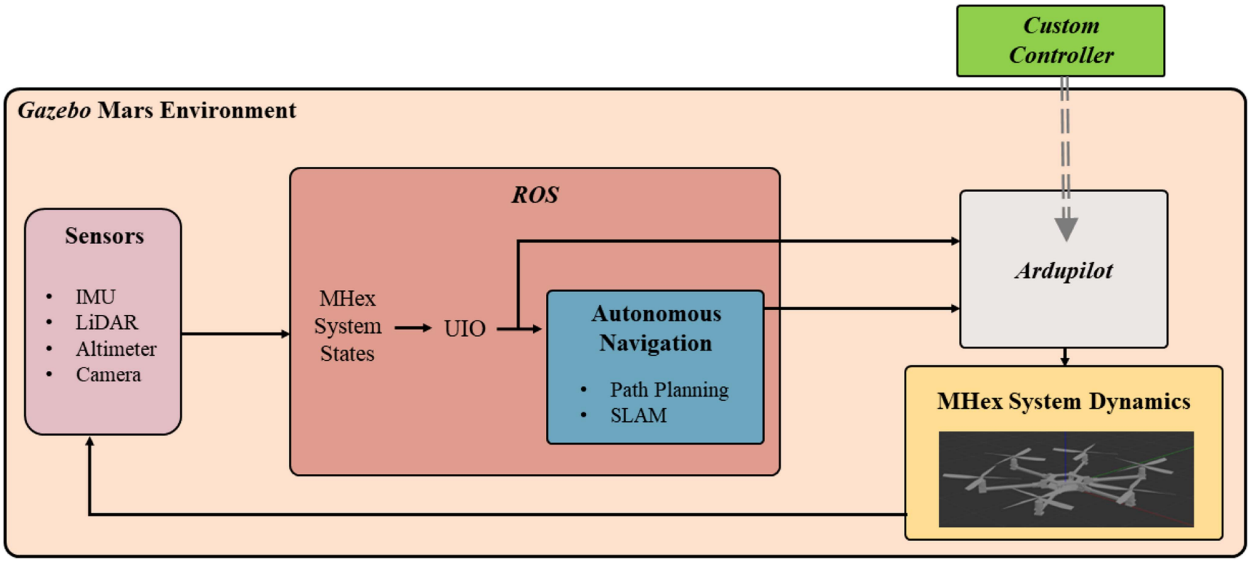

Fig. 5. Simulator architecture.

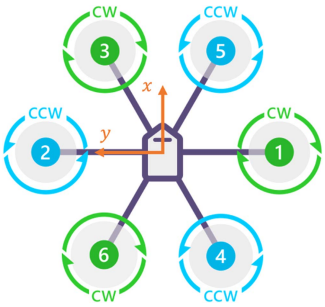

Fig. 6. Ardupilot Hexacopter *X* configuration. Readapted from [40].

spinning sensor is modeled and attached to the MHex body to account for its additional dynamics.

III. GNC SYSTEM

As previously described, the MHex can explore harsh environments and remote areas otherwise denied to ground vehicles. For this reason, it requires a robust GNC system to perform precise GPS-denied autonomous navigation and advanced control stability. Moreover, in complex scenarios, such as the Martian terrain, both stability and overall performance must go along with the robustness of the MHex against external and unknown disturbances acting on the system. A well-known category of filters developed in the last decades to address such issues refers to Kalman filters. Particularly, a wide range of applications includes the extended Kalman filter (EKF) thanks to its simplicity and versatility in many operative contexts. Kalman filters provide an optimal estimation bounded under the strong assumption of Gaussian noise distribution, such as a complex tuning of parameters and covariance matrices, especially with high-dimensional systems.

The UIO is an estimator that combines an easier design and robustness to modeling uncertainties in the system dynamics when compared to different types of filters and observers [41]. Indeed, as further shown in Section III-A1, the UIO performances are higher than for the corresponding EKF, as it efficiently handles unknown external disturbances (e.g., wind gusts) together with good management of sensors' noise, guaranteeing the asymptotic convergence of the estimation error without prior assumptions of noise distribution or bounded unknown input signals, thus overcoming the limitations of the Kalman filters. Fig. 7 provides the GNC framework for the MHex. In the proposed system, the *perception and estimation* block collects the measurements coming from a 3-D LiDAR, a downward laser altimeter, a tracking camera, and the onboard IMU to obtain partial information about the MHex's state through the sensor fusion of different odometry estimations [LiDAR inertial odometry (LIO), and visual inertial odometry, (VIO)]. Then, the UIO estimates both the unknown inputs of the dynamic system, which are not directly measured by the onboard sensors, and the full state of the MHex. The *planning* block performs the optimal trajectory given a series of waypoints sent from the ground station, and the SLAM algorithm allows for the autonomous mapping of the surrounding environment, in turn sending feedback to the path planner for trajectory optimization. The *controller* block computes the control action required to steer the MHex along the desired trajectory. Given the underactuated property of multirotors, the control structure is divided in outer (*position*) and inner (*attitude*) loop. The stock position controller within Ardupilot computes the attitude trajectory to reach the mission waypoints while the custom deployed inner loop controller provides the control action for attitude tracking. The following paragraph provides an in-depth analysis of the first two blocks, while the control strategies are discussed in paragraph III-B.

A. Autonomous Navigation Strategy

1) *Unknown Input Observer Design:* Single-sensor SLAM systems are usually fragile and full of uncertainty

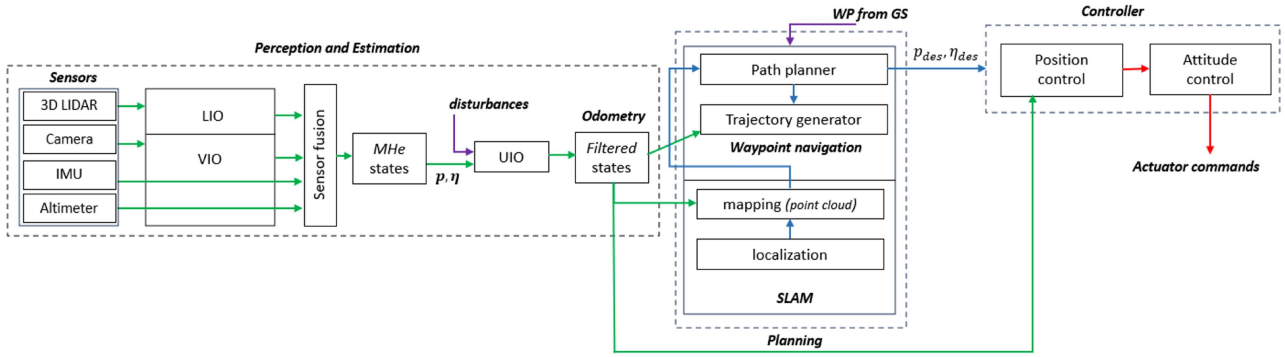

Fig. 7. GNC subsystem: Perception and estimation, planning and control frameworks.

when performing localization. Considering the complexity of the mission when performing autonomous navigation, the MHex carries onboard three different sensors to perform precise SLAM, as shown in Fig. 7. Multisensor fusion approach merges incoming information from the three sensors into a single, consistent estimate of the full MHex state by separately processing measurement data of each sensor and fusing them to achieve the latest state estimation. In the proposed scheme, LIO uses point cloud data to obtain both the MHex pose estimation and the 3-D map of the environment, while VIO is in charge of achieving the pose estimation by combining visual sensor data and IMU data. The fusion of these two pieces of information, together with laser altimeter data for a more accurate altitude state, allows for an accurate estimation of the MHex state.

After obtaining preliminary information on the system with the onboard sensors, the UIO handles disturbances acting on the MHex and not directly measurable, such as external wind disturbances, as well as sensor bias, and estimates the final MHex's states to be used for navigation and control. In the design of the UIO [42], [43], the state estimation process is decoupled from the unknown inputs, the latter reconstructed once the state estimation convergence is obtained. Following the reasoning in [12], the linearized MHex system can be modeled in matrix form as

$$\begin{aligned} \dot{x} &= A\,x + B\,u + W\,\delta \\ y &= C\,x + D\,u + H\,\delta \end{aligned} \tag{4}$$

where $x \in \mathbb{R}^n$ is the state vector, $u \in \mathbb{R}^p$ and $\delta \in \mathbb{R}^v$ are the known and unknown input vectors, respectively, $y \in \mathbb{R}^c$ is the output vector, and A, B, C, D, W, and H are matrices of suitable dimensions. Without loss of generality, matrices D and H in (4) are assumed null, thus the output matrix only depends on the state.

Considering the Lth Taylor series vectors U^L and Γ^L of the known and unknown inputs, i.e., $u(t)$ and $\delta(t)$, the Lth system's response vector is given by

$$Y^L = CA^L\,x + \sum_{i=0}^{L-1} CA^{L-1-i}\left(B\,u^{(i)} + W\,\delta^{(i)}\right) \tag{5}$$

then, in the compact form

$$Y^L = O^L\,x + J_u^L\,U^L + J_\gamma^L\,\Gamma^L \tag{6}$$

where O^L is the Lth order observability matrix, while J_u^L and J_γ^L are the Lth order invertibility matrices corresponding to the known and unknown input signals. In this setting, following the analytical reasoning described in [43], an UIO for the system in (4) is given by

$$\dot{\hat{x}} = E\,\hat{x} + F\left(Y^L - J_u^L\,U^L\right) + B\,u \tag{7}$$

with E and F being two design matrices. Considering (6), a direct computation of the state estimation error dynamics, i.e., $\dot{\tilde{x}} = \dot{\hat{x}} - \dot{x}(t)$, leads to

$$\begin{aligned} \dot{\tilde{x}} &= E\,\hat{x} + F\left(Y^L - J_u^L\,U^L\right) + B\,u - A\,x - B\,u - W\,\delta \\ &= E\,\tilde{x} + F\left(Y^L - J_u^L\,U^L\right) + (E - A)\,x - W\delta \\ &= E\,\tilde{x} + F\,O^L\,x + F\,J_\gamma^L\,\Gamma^L + (E - A)\,x - W\delta \\ &= E\,\tilde{x} + \left(F\,O^L + E - A\right)x + F\,J_\gamma^L\,\Gamma^L - W\,\delta \end{aligned} \tag{8}$$

and it is proved that, if the following conditions are simultaneously satisfied:

$$\begin{aligned} F\,J_\gamma^L &= \left[W,\, 0_{n\times v}\right] \\ E &= A - F\,O^L \end{aligned} \tag{9}$$

the estimation error dynamics takes the form

$$\dot{\tilde{x}} = E\,\tilde{x}. \tag{10}$$

Finally, by virtue of an appropriate choice of the matrix E, the system in (10) can be made convergent to zero. The solvability of the above conditions can be satisfied if and only if (4) is invertible and strong observable, i.e., for some $L \leq n$ must hold

$$\operatorname{rank}\left(J_\gamma^L\right) = v + \operatorname{rank}\left(J_\gamma^{L-1}\right) \tag{11}$$

$$n = \operatorname{rank}\left(\left[O^L, J_\gamma^L\right]\right) - \operatorname{rank}\left(J_\gamma^L\right). \tag{12}$$

2) *3-D LiDAR Mapping and Odometry:* As described in the GNC framework of Fig. 7, the *Planning* block is in charge of implementing the SLAM process along with the path planning algorithm. 3-D LiDARs permit to capturing of fine details of wide environments without being affected by variable illumination conditions. The SLAM method is also preferred in the context of the mission because of the complexity of autonomous navigation in a GPS-denied environment; thus, a dedicated localization and mapping technique is required from the MHex to perform the mission

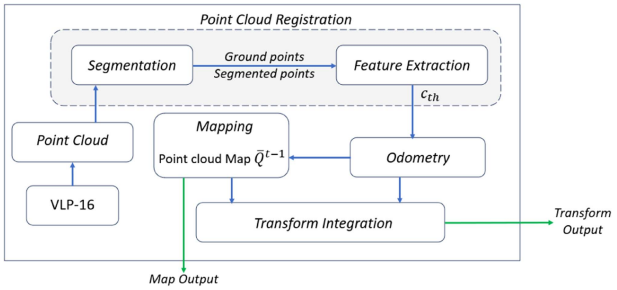

Fig. 8. 3-D LiDAR odometry and mmapping system overview.

tasks. The SLAM framework implemented onboard the MHex is shown in Fig. 8. The SLAM system receives data input from the VLP-16 LiDAR and then generates outputs regarding the computed map (*map output*) and the pose with respect to the generated map (*transform output*). The overall SLAM system is divided into four modules: In the *point cloud registration* module, the *segmentation* takes the scan's point cloud $P_t = \{p_1, p_2, \ldots, p_n\}$ acquired at time t and, based on the VLP-16 horizontal and vertical resolution (0.2° and 2°) projects it onto a range image of resolution 1800 by 16. The points p_i in the point cloud are then represented in the range image by a unique pixel with a corresponding Euclidean distance r_i from the sensor. A second level of clustering is applied to the range image and the selected points are grouped into different clusters of 50 points each. A final selection only keeps and saves features of characteristic points (ground points and segmented points) in the range image allowing for an efficient computation of the entire data processing. In the *feature extraction* module the selected points are processed and sorted based on their roughness c with respect to a threshold c_{th}

$$c = \frac{1}{|S|.||r_i||} \left|\left| \sum_{j \in S, j \neq i} (r_j - r_i) \right|\right| \tag{13}$$

where S is the points set. Points for which $c > c_{\text{th}}$ are classified as *edge features*, while *planar features* for c smaller than c_{th} are then saved in two different sets F_e and F_p. In the *odometry* module, the sensor motion is estimated between two consecutive scans by finding the corresponding features between points in the feature sets and the ones collected in the previous scan. The odometry algorithm performs at a high frequency (but low fidelity) to estimate the LiDAR's velocity, while the *mapping* algorithm runs at a lower frequency for fine matching of features in the set $\{F_e, F_p\}$ to a surrounding wider point cloud map Q^{t-1} and further registration of the point cloud. For a better computation of data, each feature set is stored in Q^{t-1} instead of a single point. Each feature set is associated with the pose of the LiDAR when the scan is taken, considering the sensor field of view (FoV), and the selected feature sets are then transformed and fused into Q^{t-1}.

B. Controllers

This section briefly describes the control algorithms applied to the MHex. For the study case in analysis, the Ardupilot stock PID (*A*-PID) attitude controller [21] is compared through closed-loop simulations with custom deployed PID with feedback linearization (PID-*FL*) and *backstepping* (*BC*) controllers.

1) *PID-FL:* PID is one of the most common controllers in literature and industry due to its straightforward implementation and ease of tuning, including model-based dynamic compensation into the loop which has been shown to further improve tracking performance [39]. To this end, feedback linearization is used to exactly linearize the MHex nonlinear dynamics. As such, the commanded torque vector is written as

$$\tau_c = J(\eta)v + C_\tau(\eta, \dot{\eta})\dot{\eta} \tag{14}$$

so that the closed-loop system becomes

$$\ddot{\eta} = v \tag{15}$$

which correspond to the following linear system:

$$\dot{x} = Ax + Bv \tag{16}$$

where

$$A = \begin{bmatrix} 0_{3\times3} & I_{3\times3} \\ 0_{3\times3} & 0_{3\times3} \end{bmatrix}, B = \begin{bmatrix} 0_{3\times3} \\ I_{3\times3} \end{bmatrix}, x = \begin{bmatrix} \eta \\ \dot{\eta} \end{bmatrix} \tag{17}$$

hence, the virtual control vector v becomes the control action to be designed [44]. To show the performance improvement, the feedback linearization is placed in cascade to the Ardupilot attitude PID controller and, as such, the *A*-PID output value is assigned to v.

To be noted: the feedback linearization is performed using the nonlinear attitude model (3).

2) *Backstepping:* *BC* model-based control has been shown to be very effective in controlling nonlinear system in presence of noise and external disturbances [45]. The following *BC* controller is presented in [46], for brevity, only the commanded torque is listed here

$$\tau_{c,\text{BC}} = J\left(\ddot{\eta}_d - \Lambda^2 e\right) + C_\tau\left(\dot{\eta}_d + \Lambda e\right) + K_r r + K_i \int_0^t r dt \tag{18}$$

with orientation tracking error $e = \eta_d - \eta$; sliding mode error $r = \dot{e} + \Lambda e$; and Λ, K_r, and K_i gain matrices to be tuned.

IV. SIMULATED EXPERIMENTS

In the simulated mission scenario, the MHex performs the autonomous navigation along with SLAM given a series of waypoints sent from the ground control station. The takeoff is performed in the proximity of the crater region, having as the main focus the mapping of both the entire crater and surroundings. The MHex is required to perform collision-free flights during the mapping process, thus without prior information, and landing at the goal point when the last waypoint is reached. Table V gives the aerodynamic coefficients used to simulate the lift and drag experienced by the MHex during flight.

TABLE V
MHex Aerodynamic Parameters

Parameters	α_0	α_{st}	CL_α	CD_α	VLP-*16 spin*
Value	0.0175	0.1920	7.791	0.55	1 Hz

TABLE VI
UIO and EKF RMSE, *Simulink* Comparison

RMSE	*Position*	*Orientation*	*Linear vel*	*Ang vel*
UIO	0.18	0.09	0.25	0.47
EKF	0.31	0.30	2.87	0.48

1) *Observer Validation:* As a first validation step, the comparison between the EKF and the UIO is implemented in Matlab/Simulink along a helix-based trajectory. For the EKF, the equivalent noise considered in the simulation follows a Gaussian distribution with $\mu = 0$ and variance $\sigma^2 = 0.01$, corresponding to the realistic sensor noise for both the t265 camera and the VLP liDAR. Wind acting on the system is simulated along the horizontal and vertical directions. The modeling of the wind is also applied in the second validation step with ROS and Gazebo, as follows. Then, the UIO is implemented along with the MHex system. To reach the form of (4), analytical calculations lead to the matrices

$$A = \begin{bmatrix} 0_{6\times6} & I_{6\times6} \\ 0_{6\times6} & 0_{6\times6} \end{bmatrix} \qquad B = \begin{bmatrix} M & 0_{3\times3} \\ 0_{3\times3} & J \end{bmatrix} \tag{19}$$

$$C = \begin{bmatrix} I_{6\times6} & 0_{6\times6} \end{bmatrix} \qquad W = \begin{bmatrix} 0_{6\times6} & I_{6\times6} \end{bmatrix}. \tag{20}$$

The state vector x includes the inertial position p, orientation η, and their respective derivatives $\dot{p}$, $\dot{\eta}$. Only the pose (position and orientation) is taken as the system's output, while $\dot{p}$ and $\dot{\eta}$ are estimated through the observer. According to (11) and (12), the smallest integer satisfying the above condition is $L = 2$, with the invertibility and observability matrices assuming the form

$$J^2 = \begin{bmatrix} 0 & 0 & 0 \\ CW & 0 & 0 \\ CAW & CW & 0 \end{bmatrix}, O^2 = \begin{bmatrix} C \\ CA \\ CA^2 \end{bmatrix} \tag{21}$$

for which it holds, based on (19), (20), rank$(J) = 6$ and rank$(O) = 12$, thus satisfying the conditions of solvability.

The state estimation error for the EKF and the UIO is given in Fig. 9 The UIO tracks the states even in the presence of external disturbances and more effectively than the EKF. Even in the presence of sensor bias, the UIO demonstrates robustness to the noise maintaining an accurate estimate of the states and a corresponding smaller error magnitude, also not requiring any information about the unknown inputs, here in the form of external disturbance. The computed root mean square error (RMSE) for both the EKF and the UIO is given in Table VI.

As a second validation step, based on the results gained from the analysis in Matlab/Simulink, the UIO is tested in the simulator architecture in order to both test and assess the algorithm's robustness to external disturbances and

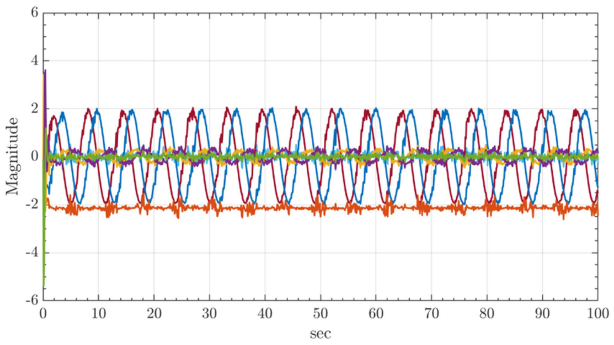

(a)

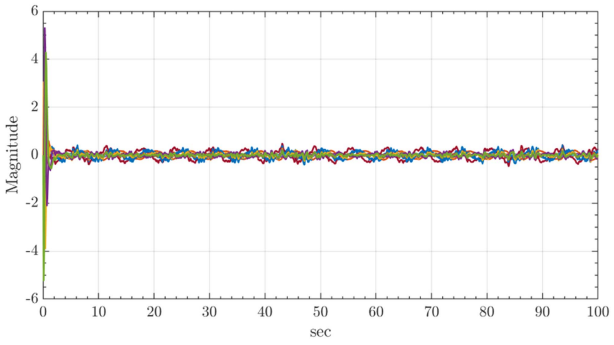

(b)

Fig. 9. UIO and EKF comparison. (a) EKF state estimation error. (b) UIO state estimation error.

TABLE VII
UIO RMSE, *Simulator*

UIO estimate	*Position*	*Orientation*	*Linear vel*	*Ang vel*
RMSE	0.22	0.72	0.23	0.11

TABLE VIII
MHex Controllers RMSE, *Simulator*

RMSE [deg]	*A*-PID	PID *FL*	*BC*
No Wind	4.23	1.82	3.78
Wind	9.36	1.37	3.96

measurement uncertainties, and to obtain a software-in-the-loop validation of the proposed system implementation. The simulation results carried out in the simulator for the analyzed mission are presented in Table VII and Fig. 10. The wind is applied along the horizontal direction ($\bar{v}_w$) with a maximum intensity of 4 m/s, and vertically up to 1 m/s ($\bar{v}_{w,z}$). As shown, the UIO is able to estimate the unknown states of the system (velocities), having the pose as input. The estimated states closely track the original states without significant drift or deviation from the reference, with the most significant impact during the landing phase. The overall accuracy of the proposed method is validated by the RMSE measurements.

2) *Controller Comparison:* Table VIII gives the comparison between the RMSE of the attitude with respect to desired attitude trajectory along with the different control approaches implemented. Two different simulated experiments are performed in the simulator architecture: in the first, only the sensor noises are taken into account without

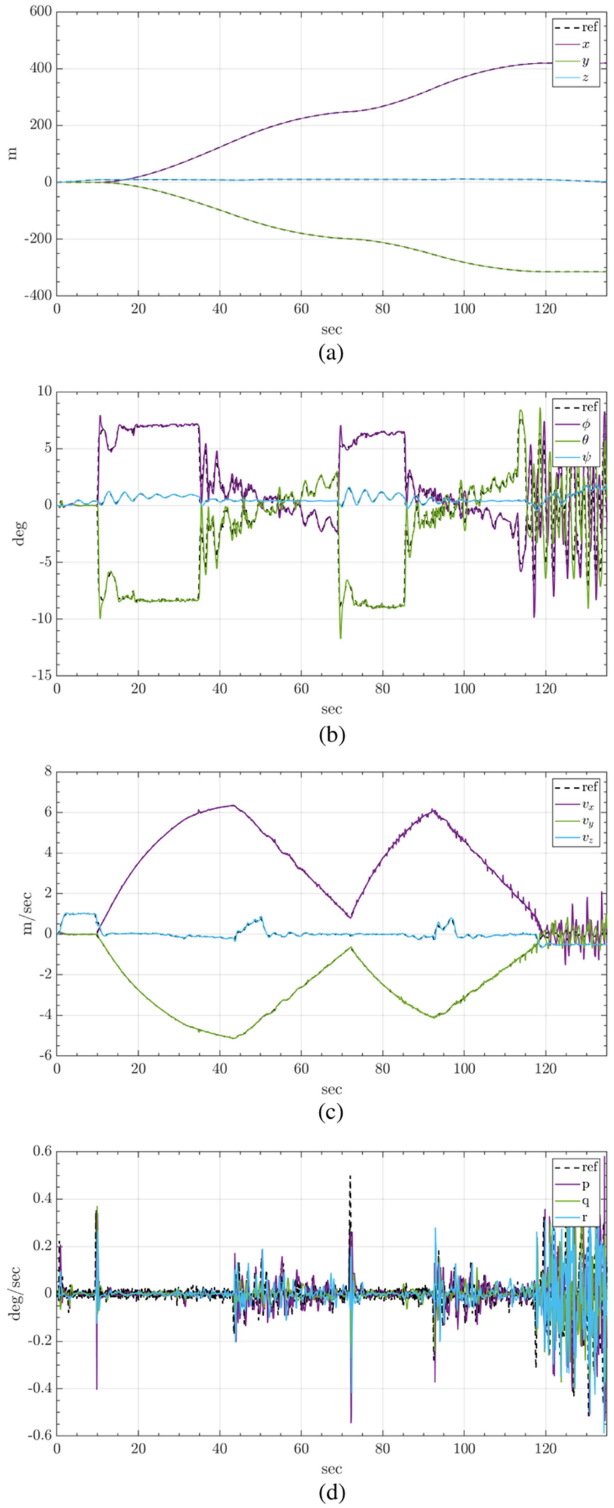

Fig. 10. UIO state estimation. (a) Position. (b) Orientation. (c) Linear velocity. (d) Angular velocity.

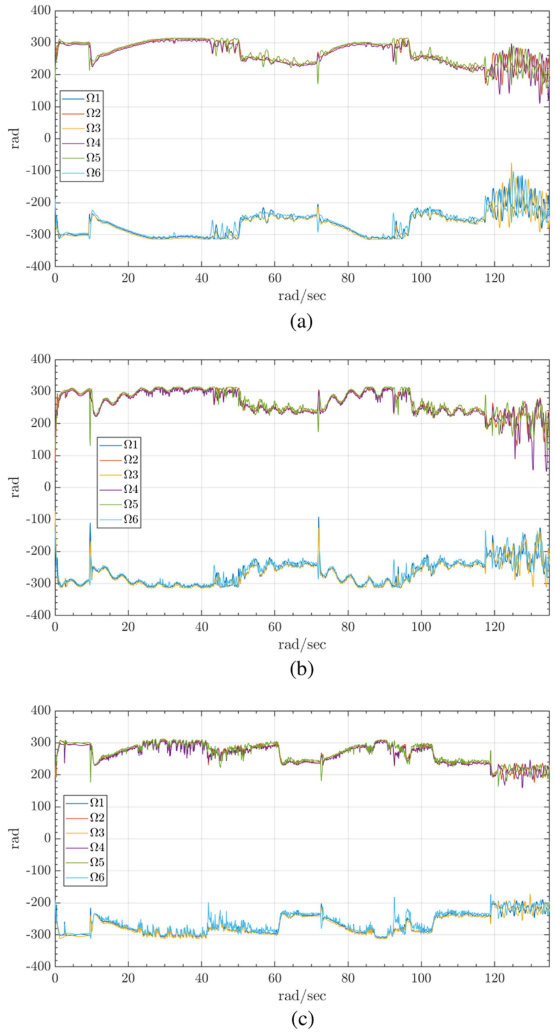

Fig. 11. MHex propeller angular velocity, simulated experiment including wind. (a) *A*-PID. (b) PID-*FL*. (c) *BC*.

other external disturbances, testing smooth flight conditions. In the second one, both wind along horizontal ($\bar{v}_w$) and vertical ($\bar{v}_{w,z}$) directions and sensor bias are considered.

As shown, the model-based control approaches are able to achieve smaller RMSE compared to the *A*-PID controller. The propeller angular velocity during cruise remains in the range of $M = 0.55$ to 0.8 at tip, corresponding to 1910 to 2780 r/min [200 rad/s to 291 rad/sec, respectively, with max peaks of 315 rad/sec (3008 r/min, M = 0.86)]. Considering the flight speed as ground speed, the limit of 8 m/s guarantees that the linear velocity at the propeller tip is less than $M = 0.89$. The propeller angular velocity has an average of 260 rad/sec (2483 r/min, M = 0.71), and a median of 265 rad/s (2531 r/min, $M = 0.73$), resulting close to the blade optimum operating point of $M = 0.75$, based on the data available in [8], as shown in plots in Table IX. The resulting control gains for each controller show the ability of the tuning process to achieve the best performances while avoiding saturation of the control action, while the propeller rates, displayed in Fig. 11 remain bounded and stable for all controller strategies. Finally, given the overall better performance, even during wind simulations, the model-based approaches are preferable for mapping and navigation tasks.

3) *Mapping Experiment:* Fig. 10 shows the mapping process in the explored site based on the point cloud feature extraction. As reported in Section III-A2, when performing SLAM both the edge and planar features are extracted from

TABLE IX
Controller Gains

Gains *PID*	$K_{p,prefilter}$	K_p	K_i	K_d
PID-AP	$4.5 \times I_{3\times3}$	diag(0.135, 0.135, 0.180)	diag(0.135, 0.135, 0.018)	diag(0.0036, 0.0036, 0)
PID-FL	$9 \times I_{3\times3}$	diag(1.25, 1.25, 0.50)	$0.1 \times I_{3\times3}$	diag(0.01, 0.01, 0)
Gains *BC*	K_r	K_i	Λ	$--$
BC	$1 \times I_{3\times3}$	$30 \times I_{3\times3}$	$1 \times I_{3\times3}$	$--$

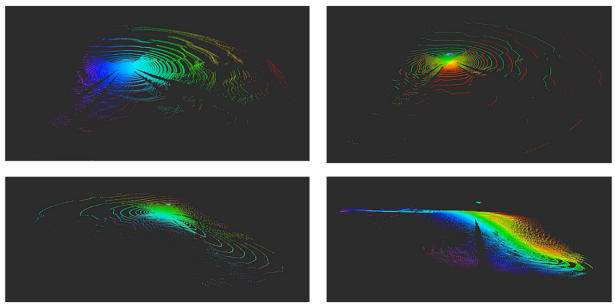

Fig. 12. MHex mapping framework: The MHex approaches the crater and performs the point cloud map. Edge and planar features are progressively extracted, and selected subsets of points are then stored in the final map.

the same LiDAR scan, and the corresponding feature subset is first optimized through point cloud segmentation and then processed by the mapping module. This procedure allows for a reduction of the number of points stored in the map, also filtering out unstable features based on the c_{th} threshold. The SLAM algorithm is able to track morphological features of the crater while performing real-time pose estimation. The VLP-16 provides precise and direct depth measurements in the environment, resulting in accurate 3-D point cloud data even in a wide and feature-poor scenario such as Martian terrain. Moreover, since the entire mapping process results optimized in terms of ground point cloud segmentation, the liDAR-mapping accuracy is improved, reducing the computational complexity when compared to the vision-based counterpart. Last but not least, the LiDAR FoV results in a wide range of collecting data, thus particularly valuable when a thorough comprehension of the environment is essential during long-range exploration.

V. CONCLUSION

This article presented a system analysis for a future Martian hexacopter. After deriving a conceptual architecture and sizing of the MHex prototype, autonomous navigation based on a realistic mission scenario along with SLAM and 3-D mapping showed the capability of accurate mapping and stratigraphic investigation of the surrounding environment, addressing the numerous challenges of Martian flight together with the comparison of different control strategies. To validate the entire GNC analysis, a simulator architecture based on free and open-source software (ROS, Gazebo, and Ardupilot) was proposed, and the simulated experiments considering both state estimation and model-based control were performed with promising results. Realistic software in the loop (SITL) features included, along with Martian environmental conditions, sensor noises, aerodynamic and wind effects, VLP-16 LiDAR rotating dynamics, GPS-denied position estimates, and conservative sampling rates. First, an enhanced UIO was presented and compared to the well-known EKF for filtering sensor output, showing robustness against disturbances and sensor bias, guaranteeing accurate estimates of the unknown states and overcoming the limitations of different classes of filters more sensitive to external disturbances. Second, a comparison between model-based control strategies (PID-*FL* and *BC*) and the stock Ardupilot attitude PID controller (*A*-PID) showed the advantage of considering the MHex nonlinear dynamics for achieving a more precise control and compensating for the tight flight envelope and environmental conditions characterizing the flying on Mars. Finally, even if experimental verification of both rotor structural design and aerodynamic performance is required to validate the entire MHex architecture, the presented examination of the hexacopter gave consistency and substantial capability for autonomous operation on Mars in the context of future exploration. Moreover, the Ardupilot integration (or any other flight controller unit) in the simulator pipeline will allow for reducing the effort required to transition from SITL to hardware in the loop. The authors intend to share the code and documentation to enable other researchers to test their applications on the presented simulator architecture.

REFERENCES

[1] J. Simon et al., "Samples collected from the floor of Jezero crater with the Mars 2020 perseverance rover," *J. Geophysical Res.: Planets*, vol. 128, no. 6, 2023, Art. no. e2022JE007474.

[2] J. Balaram, M. Aung, and M. P., "Golombek the ingenuity helicopter on the perseverance rover," *Space Sci. Rev.*, vol. 217, no. 4, 2021, Art. no. 56.

[3] T. Tzanetos et al., "Ingenuity Mars helicopter: From technology demonstration to extraterrestrial scout," in *Proc. IEEE Aerosp. Conf.*, 2022, pp. 01–19.

[4] G. Kminek, M. A. Meyer, D. W. Beaty, B. L. Carrier, T. Haltigin, and L. E. Hays, "Mars sample return (MSR): Planning for returned sample science," *Astrobiology*, vol. 22, no. S1, pp. S–1, 2022.

[5] F. Mier-Hicks et al., "Sample recovery helicopter," in *Proc. IEEE Aerosp. Conf.*, 2023, pp. 1–11.

[6] L. Sopegno, K. P. Valavanis, M. J. Rutherford, and L. Casalino, "Mars sample return mission: Mars ascent vehicle propulsion design," in *Proc. IEEE Aerosp. Conf.*, 2020, pp. 1–9.

[7] A. Elsaesser et al., "Future space experiment platforms for astrobiology and astrochemistry research," *npj Microgr.*, vol. 9, no. 1, 2023, Art. no. 43.

[8] W. Johnson et al., "Mars science helicopter conceptual design," Ames Res. Center, NASA, Mountain View, CA, USA, Tech. Rep. NASA/TM-2020-220485, 2020.

[9] J. Balaram, I. Daubar, J. Bapst, and T. Tzanetos,, "Helicopters on mars: Compelling science of extreme terrains enabled by an aerial platform," in *Proc. 9th Int. Conf. Mars*, 2019, Art. no. 6277.
[10] T. Tzanetos et al., "Future of mars rotorcraft—Mars science helicopter," in *Proc. IEEE Aerosp. Conf.*, 2022, pp. 1–16.
[11] H. F. Grip et al., "Guidance and control for a Mars helicopter," in *Proc. AIAA Guid., Navigation, Control Conf.*, 2018, Art. no. 1849.
[12] S. Pedone, M. Trumić, K. Jovanović, and A. Fagiolini, "Robust and decoupled position and stiffness control for electrically-driven articulated soft robots," *IEEE Robot. Automat. Lett.*, vol. 7, no. 4, pp. 9059–9066, Oct. 2022.
[13] H. Lu, H. Shen, B. Tian, X. Zhang, Z. Yang, and Q. Zong, "Flight in GPS-denied environment: Autonomous navigation system for micro-aerial vehicle," *Aerosp. Sci. Technol.*, vol. 124, 2022, Art. no. 107521.
[14] J. Zhang and S. Singh, "LOAM: LiDAR odometry and mapping in real-time," in *Proc. Robot.: Sci. Syst.*, Berkeley, CA, 2014, pp. 1–9.
[15] T. Shan and B. Englot, "LeGO-LOAM: Lightweight and ground-optimized LiDAR odometry and mapping on variable terrain," in *Proc. IEEE/RSJ Int. Conf. Intell. Robots Syst.*, 2018, pp. 4758–4765.
[16] T. H. Chan, H. Hesse, and S. G. Ho, "LiDAR-based 3D SLAM for indoor mapping," in *Proc. 7th Int. Conf. Control, Automat. Robot.*, 2021, pp. 285–289.
[17] X. Xu et al., "A review of multi-sensor fusion SLAM systems based on 3D LiDAR," *Remote Sens.*, vol. 14, no. 12, 2022, Art. no. 2835.
[18] R. Milijas, L. Markovic, A. Ivanovic, F. Petric, and S. Bogdan, "A comparison of LiDAR-based SLAM systems for control of unmanned aerial vehicles," in *Proc. Int. Conf. Unmanned Aircr. Syst.*, 2021, pp. 1148–1154.
[19] A. Patel, A. Banerjee, B. Lindqvist, C. Kanellakis, and G. Nikolakopoulos, "Design and model predictive control of a Mars coaxial quadrotor," in *Proc. IEEE Aerosp. Conf.*, 2022, pp. 1–11.
[20] S. Dutta, C. D. Karlgaard, D. Kass, M. Mischna, and G. G. Villar, "III postflight analysis of atmospheric properties from Mars 2020 entry, descent, and landing," *J. Spacecraft Rockets*, vol. 60, no. 3, pp. 1022–1033, 2023.
[21] "Ardupilot Copter attitude control," [Online]. Available: https://ardupilot.org/dev/docs/apmcopter-programming-attitude-control-2.html
[22] C. Vleugels, B. Foing, and O. Swida, "A comparison of perseverance rover and HiRISE data: Site interpretations in Jezero crater copernicus meetings," Eur. Geosciences Union, Munich, Germany, Tech. Rep. EGU23-320, 2023.
[23] V. Z. Sun and K. M. Stack, "Geologic map of Jezero crater and the Nili planum region, mars," U.S. Geological Surv., Reston, VA, USA, Scientific Investigations Map 3464, 2020. [Online]. Available: https://api.semanticscholar.org/CorpusID:229665623
[24] V. Zappek, M. Rinker, L. Daxer, and M. Hajek, "Evaluation of aerial vehicle configurations for high-range Mars missions," *CEAS Space J.*, vol. 15, pp. 761–775, 2023.
[25] L. Sopegno, P. Livreri, and K. Valavanis, "Using UAVs for future mission on Mars," in *Proc. Int. Astronautical Congr.*, 2022, pp. 1–11.
[26] M. Radotich, "A study of past, present, and future mars rotorcraft," in *Proc. 9th Biennial Auton. VTOL Tech. Meeting*, 2021, pp. 1–17. [Online]. Available: https://api.semanticscholar.org/CorpusID:234777444
[27] P. G. Jayasekara, G. Ishigami, and T. Kubota, "Testing and validation of autonomous navigation for a planetary exploration rover using opensource simulation tools," in *Proc. Int. Symp. Artif. Intell., Robot. Automat. Space*, 2012, pp. 1–8.
[28] J. I. Giribet, R. S. Sanchez-Pena, and A. S. Ghersin, "Analysis and design of a tilted rotor hexacopter for fault tolerance," *IEEE Trans. Aerosp. Electron. Syst.*, vol. 52, no. 4, pp. 1555–1567, Aug. 2016.
[29] Hovermap (2023), "Hovermap 3D LiDAR," Accessed: Sep. 2023. [Online]. Available: https://im-mining.com/2019/02/02/emesent-hovermap-first-autonomous-liDAR-mapping-payload-mining-drones/
[30] D. R. Cremons, "Cremons: The future of LiDAR in planetary science," *Front. Remote Sens.*, vol. 3, 2022, Art. no. 1042460.
[31] P. Lee, E. Kommedal, A. Horchler, E. Amoroso, K. Snyder, and A. Birgisson, "Lofthellir lava tube ice cave, Iceland: Subsurface micro-glaciers, rockfalls, drone LiDAR 3D-mapping, and implications for the exploration of potential ice-rich lava tubes on the Moon and Mars," in *Proc. 50th Annu. Lunar Planet. Sci. Conf.*, 2019, Art. no. 3118.
[32] F. Amzajerdian, D. Pierrottet, G. D. Hines, L. Petway, B. Barnes, and J. M. Carson, "Development of navigation Doppler LiDAR for future landing missions," in *Proc. AIAA SPACE*, 2016, Art. no. 5590.
[33] I. Velodyne, "LiDAR velodyne VLP-16 LIDAR," 2023, datasheet.
[34] "IntelRealSense t256 tracking camera," datasheet camera. Accessed: Sep. 2023.
[35] Garmin (2023), "Altimeter garmin V3 lite," Accessed: Sep. 2023. [Online]. Available: https://www.garmin.com/en-US/blog/general/garmin-on-mars/
[36] P. Li, D. Liu, X. Xia, and S. Baldi, "Embedding adaptive features in the ardupilot control architecture for unmanned aerial vehicles," in *Proc. IEEE 61st Conf. Decis. Control*, 2022, pp. 3773–3780.
[37] P. Li, D. Liu, and S. Baldi, "Adaptive integral sliding mode control in the presence of state-dependent uncertainty," *IEEE/ASME Trans. Mechatron.*, vol. 27, no. 5, pp. 3885–3895, Oct. 2022.
[38] S. Baldi, D. Sun, X. Xia, G. Zhou, and D. Liu, "ArduPilot-based adaptive autopilot: Architecture and software-in-the-loop experiments," *IEEE Trans. Aerosp. Electron. Syst.*, vol. 58, no. 5, pp. 4473–4485, Oct. 2022.
[39] S. Martini, S. Sönmez, A. Rizzo, M. Stefanovic, M. J. Rutherford, and K. P. Valavanis, "Euler–Lagrange modeling and control of quadrotor UAV with aerodynamic compensation," in *Proc. Int. Conf. Unmanned Aircr. Syst.*, 2022, pp. 369–377.
[40] Ardupilot, "Ardupilot copter," Accessed: Sep. 2023. [Online]. Available: https://ardupilot.org/copter/docs/common-autopilots.html
[41] S. I. Azid, K. Kumar, M. Cirrincione, and A. Fagiolini, "Robust motion control of nonlinear quadrotor model with wind disturbance observer," *IEEE Access*, vol. 9, pp. 149164–149175, 2021.
[42] S. Pedone and A. Fagiolini, "Racecar longitudinal control in unknown and highly-varying driving conditions," *IEEE Trans. Veh. Technol.*, vol. 69, no. 11, pp. 12521–12535, Nov. 2020.
[43] S. Sundaram and C. N. Hadjicostis, "Delayed observers for linear systems with unknown inputs," *IEEE Trans. Autom. Control*, vol. 52, no. 2, pp. 334–339, Feb. 2007.
[44] B. Siciliano, L. Sciavicco, L. Villani, and G. Oriolo, *Robotics: Modelling, Planning and Control*. Berlin, Germany: Springer Sci. & Business Media, 2010.
[45] S. Martini, M. Stefanovic, A. Rizzo, M. J. Rutherford, P. Livreri, and K. P. Valavanis, "A benchmark framework for testing, evaluation, and comparison of quadrotor linear and nonlinear controllers," in *Proc. Int. Conf. Unmanned Aircr. Syst.*, 2023, pp. 471–478.
[46] A. Das, F. Lewis, and K. Subbarao, "Backstepping approach for controlling a quadrotor using Lagrange form dynamics," *J. Intell. Robotic Syst.*, vol. 56, no. 1, pp. 127–151, 2009.

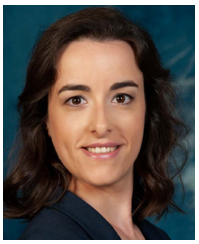

Laura Sopegno received the master's degree in aerospace engineering, space, and propulsion systems with the Polytechnic of Turin, Turin, Italy, in 2019. She is currently working toward the Ph.D. degree in electrical and computer engineering with the Engineering Department, University of Palermo, Palermo, Italy, and the Electrical and Computer Engineering Department, University of Denver, Denver, CO, USA.

She worked on the Mars Sample Return mission with Thales Alenia Space Company, Rome, Italy, from 2020 to 2021. Her research interests include propulsion systems for space applications to the autonomous guidance, navigation and control architectures of unmanned aerial vehicles with a principal focus on future Mars and Moon exploration.

Simone Martini received the B.S. degree in aerospace engineering and the M.S. degree in mechatronics engineering from Politecnico di Torino, Torino, Italy, in 2019 and 2020, respectively. He is currently working toward the Ph.D. degree in electrical and computer engineering with the Electrical and Computer Engineering Department, University of Denver, Denver, CO, USA.

From 2022 to 2023, he worked in collaboration with the University of Palermo, Palermo, Italy, under supervision of Dr. Livreri supported by Progetto "SEAVIEW", Azione 1.1.5, PO FESR 2014/2020. He is currently working under the supervision of Dr. Kimon P. Valavanis with the Unmanned Systems Research Institute (DU^2SRI), University of Denver, and Dr. Alessandro Rizzo with Politecnico di Torino, Turin, Italy. His research interest includes around nonlinear modeling and control of UAV.

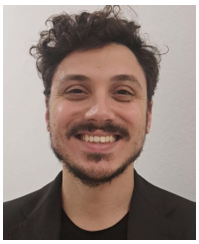

Salvatore Pedone (Member, IEEE) received the M.S. degree in aerospace engineering and the Ph.D. degree in information and communication technologies from the University of Palermo, Palermo, Italy, in 2018 and 2023, respectively.

He is currently a Researcher and Lecturer of Automatic Control with the University of Palermo. His research interests are in the design and development of control and estimation methods for complex nonlinear systems as self-driving vehicles, unmanned aerial vehicles and soft articulated–robots.

Adriano Fagiolini (Member, IEEE) received the M.S. degree in computer science engineering and the Ph.D. degree in robotics and automation from the University of Pisa, Pisa, Italy, in 2004 and 2009, respectively.

He has been a Visiting Researcher with the Department of Energy, IUT Longwy, University de Lorraine (France), Metz, France, in 2019, and the Department of Mechanical Engineering, University of California at Riverside, Riverside, CA, USA, in 2015 and 2017. He enrolled in the Summer Student Programme at the European Center for Nuclear Research, Geneva, in 2002, and in the International Curriculum Option of Doctoral studies in Hybrid control for complex, distributed, and heterogeneous embedded systems in 2007. In 2008, he led the team of the University of Pisa during the first European Space Agency's Lunar Robotics Challenge, which resulted in a second-place prize for the team. He is currently an Associate Professor with the University of Palermo, Italy.

Dr. Fagiolini. is a Member of the IFAC Technical Committee on Control and Education, since 2020. He was one of the recipients of the IEEE ICRA's Best Manipulation Paper Award, in 2005. He is an Associate Editor for the IEEE ROBOTICS AND AUTOMATION LETTERS, since 2018, of the newly launched Robotics Reports Journal by Mary Ann Liebert, since 2023, and of the IEEE International Conference on Robotics and Automation and IEEE/RSJ International Conference on Intelligent Robots, since 2017.

Matthew J. Rutherford (Member, IEEE) received the B.S. degree in civil engineering from Princeton University, in 1996 and the M.S. and Ph.D. degrees in computer science from the University of Colorado, Boulder, in 2001 and 2006, respectively.

He is currently an Associate Professor with the Department of Computer Science with a joint appointment with the Department of Electrical and Computer Engineering, University of Denver, Denver, CO, USA, where he is also the Deputy Director of the DU Unmanned Systems Research Institute (DU^2SRI). His research interests include the development of advanced controls and communication mechanisms for autonomous aerial and ground robots; applications of real-time computer vision to robotics problems using GPU-based parallel processing; testing and dynamic evaluation of embedded, real-time systems; development of complex mechatronic systems (mechanical, electrical, and software); the development of software techniques to reduce the amount of energy being consumed by hardware; development of a high-precision propulsion system for underwater robots.

Margareta Stefanovic (Senior Member, IEEE) received the Ph.D. degree in electrical engineering, control systems from the University of Southern California, Los Angeles, CA, USA, in 2005.

She is an Associate Professor with the Department of Electrical and Computer Engineering, University of Denver, Denver, CO, USA. He has coauthored the book *Safe Adaptive Control: Data-driven Stability Analysis and Robust Synthesis*(Lecture Notes in Control and Information Sciences) (Springer). Her research interests include robust adaptive control of uncertain systems, multiagent systems and distributed control.

Dr. Stefanovic serves as a Subject Editor for the *International Journal of Robust and Nonlinear Control*, Editor-at-Large for *Journal of Intelligent and Robotic Systems*, and Associate Editor for *ISA Transactions*.

Alessandro Rizzo (Senior Member, IEEE) received the laurea degree (summa cum laude) in computer engineering and the Ph.D. degree in automation and electronics engineering from the University of Catania, Catania, Italy, in 1996 and 2000, respectively.

In 1998, he was a EURATOM Research Fellow with JET Joint Undertaking, Abingdon, U.K., researching on sensor validation and fault diagnosis for nuclear fusion experiments. In 2000 and 2001, he has worked as a Research Consultant with ST Microelectronics, Catania Site, Italy, and as an Industry Professor of Robotics with the University of Messina, Messina, Italy. From 2002 to 2015, he was a tenured Assistant Professor with the Politecnico di Bari, Bari, Italy. Since 2012, he has been a Visiting Professor with the New York University Tandon School of Engineering, Brooklyn, NY, USA. In 2015, he joined Politecnico di Torino, Turin, Italy, where he is currently an Associate Professor with the Department of Electronics and Telecommunications and established the Complex Systems Laboratory. He has authored two books, two international patents, and more than 200 papers on international journals and conference proceedings. His research interests inlcude cooperative robotics, complex networks and systems, modeling and control of nonlinear systems.

Dr. Rizzo was the recipient of the Award for the Best Application Paper at the IFAC world triennial conference in 2002 and of the Award for the Most Read Papers in Mathematics and Computers in Simulation (Elsevier) in 2009, and was one of the recipients of the 2019 and 2021 Amazon Research Awards in robotics. He has also been a Distinguished Lecturer of the IEEE Nuclear and Plasma Science Society.

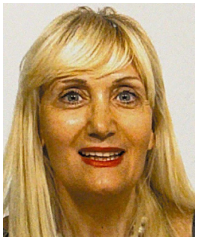

Patrizia Livreri (Senior Member, IEEE) received the laurea degree (hons.) in electronics engineering and the Ph.D degree in ICT from the University of Palermo, Italy, in 1986 and 1992, respectively.

From 1993 to 1994, she was a Researcher with CNR, Rome, Italy. Since 1994, she has been an Assistant Professor with the University of Palermo, Palermo, Italy, where she is currently a Professor of Electronics with the Department of Engineering. Since 2017, she has been the Director of the Power Electronics Laboratory. Since 2020, she has been the Director of the Microwave Power Laboratory. In 2020, she also joined the National Laboratory for Radar and Surveillance Systems, Pisa, Italy. Since 2021, she has been a Visiting Professor with the San Diego State University, San Diego, CA, USA. She has authored or coauthored more than 250 published papers and served as an invited speaker and Keynote speaker at international conferences. Her research interests include microwave power amplifiers, high power microwave source, antennas, radar, and UAV.

Dr. Livreri was the recipient of the Award for Best Paper at the IEEE ICRERA Conference in 2017. Since 2023, she has been serving as an Associate Editor for IEEE ACCESS. She has been selected to serve NATO Science and Technology Organization as an Invited Speaker for Quantum Technology. She is the Principal investigator of the Microwave Quantum Radar project, funded by the Ministry of Defense, the supervisor of many funded projects.

Kimon P. Valavanis (Senior Member, IEEE) received the Ph.D. degree in computer and systems engineering from Rensselaer Polytechnic Institute (RPI), in 1986.

He held Visiting Appointments with Dipartimento di Ingegneria Meccanica e Aerospaziale, DIMEAS, Politecnico di Torino, Turin, Italy, and he was Professeur Invit, Universit de Lorraine - Polytech Nancy, France. He is currently a John Evans Professor with the Department of ECE, D. F. Ritchie School of Engineering and Computer Science, University of Denver, Denver, CO, USA. He is also a Guest Professor with the Faculty of Electrical Engineering and Computing, University of Zagreb, Zagreb, Croatia. He has authored or coauthored more than 450 book chapters, technical journal, and transaction, referred conference, and invited papers, and authored/co-authored/edited 19 books. He has graduated 40 PhD students and more than 100 M.Sc. students. His research interests include unmanned systems, distributed intelligence systems, robotics, and automation.

Dr. Valavanis is a Fellow of the American Association for the Advancement of Science, and a Fellow of the U.K. Institute of Measurement and Control. He served as Editor-in-Chief for the *Robotics and Automation Magazine*, from 1996–2005, and since 2006, of the *Journal of Intelligent and Robotic Systems*, Springer. He also serves as co-chair of the Aerial Robotics and Unmanned Aerial Vehicles Technical Committee since 2008. He founded the International Conference on Unmanned Aircraft Systems, which he runs annually. He was a Distinguished Speaker for the IEEE Robotics and Automation Society, and a Technical Expert of the NATO Science and Technology Organization (STO). He was also selected to serve as NATO Technical Evaluator for the AVT-353 Workshop on Artificial Intelligence in the Cockpit for UAV that will take place in Torino, Italy, in April 2022. In August of 2021, he was also appointed to the NATO STO Technical Team of SAS-ET-EX Integration of Unmanned Systems into Operational Units for the duration of the Program of Work. He is also a Fulbright Scholar (Senior Lecturing & Research Award).

Open Access provided by 'Università degli Studi di Palermo' within the CRUI CARE Agreement